Diffuse-interface modeling of solute trapping in rapid solidification: Predictions of the hyperbolic phase-field model and parabolic model with finite interface dissipation

Lijun Zhang [a,*,1], Ekaterina V. Danilova [a], Ingo Steinbach [a], Dmitry Medvedev [b], Peter K. Galenko [c]

[a] *Interdisciplinary Centre for Advanced Materials Simulation (ICAMS), Ruhr-Universität Bochum, D-44801 Bochum, Germany*
[b] *Lavrentyev Institute of Hydrodynamics, Siberian Branch of Russian Academy of Sciences, Lavrentyev prosp. 15, 630090 Novosibirsk, Russia*
[c] *Friedrich-Schiller-Universität Jena, Physikalisch-Astronomische Fakultät, D-07737 Jena, Germany*

Abstract

Two recently developed phase-field models, a hyperbolic model and a parabolic model with finite interface dissipation, are employed to study the solute trapping in a Si-0.25 at.% As alloy during rapid solidification. The hyperbolic model is applied at the nanometer scale of the interface width δ. The parabolic model is derived by a coarse-graining procedure and is intended to operate with mesoscopic resolution of the interface η. The coarse-graining numerical parameters, namely interface width η and the interface permeability P, are adjusted in the parabolic model to fit the segregation coefficient calculated by the microscopic model on the nanoscale. Based on the optimal sets of η and P selected at small interface velocity, a linear relation between their logarithm values is obtained. This logarithmic relation provides a theoretical basis for choosing the appropriate values of η and P in the numerical phase-field simulation in three spatial dimensions.
© 2013 Acta Materialia Inc. Published by Elsevier Ltd. All rights reserved.

Keywords: Rapid solidification; Phase-field models; Non-equilibrium; Segregation; Solute trapping

1. Introduction

Considerable theoretical and experimental research has been devoted to the kinetic descriptions of solidification [1]. Most of this research has treated the near-equilibrium or quasi-equilibrium limits of a small growth velocity [2–4]. In these limits, either the local equilibrium condition (i.e. the condition of equal chemical potential) or the condition of equal diffusion potential are employed. By contrast, the understanding of systems far from equilibrium remains less advanced. As a simple but illustrative example of a far-from-equilibrium process, the rapid solidification of a highly undercooled melt has been frequently used for the study of non-equilibrium interface kinetics due to the simplifications resulting from the lack of coherency stress effects, and from the simple interface structure for systems with an atomically rough interface [5]. Rapid solidification occurs in many techniques in contexts such as laser-induced surface melting, spray forming and welding, in which supersaturated solid solutions, metastable compounds and glasses can form [6]. During rapid solidification, the solute may be entrapped by the rapidly moving solid–liquid interface with a quantity in concentrations that differ significantly from those given by the equilibrium phase diagram. This phenomenon is commonly referred to as "solute trapping". Due to its theoretical and technological importance, in addition to experimental investigations, the effect of solute trapping has been also

---

extensively studied theoretically using, for instance, analytical models based on a sharp or semi-sharp interface hypothesis [7–13], and phase-field simulations based on diffuse interface models [14–19].

Solute trapping can be characterized by the velocity-dependent solute segregation coefficient $k(V)$, which is defined by the ratio:

$$k(V) = \frac{\text{concentration in solid}}{\text{concentration in liquid}}\bigg|_{\text{interface}} = \frac{c_S}{c_L}\bigg|_{\text{interface}}, \qquad (1)$$

with the interface velocity V. This definition of the solute segregation in Eq. (1) is based on the sharp-interface picture. As for analytical models for describing solute trapping, two important theories are available: one is the continuous growth model (CGM) [9], while the other is the local non-equilibrium model (LNM) [11,12]. The CGM is formulated by assuming a flux balance across a moving solid–liquid interface. The V-dependent solute segregation coefficient $k(V)$ in the CGM takes the form (for dilute alloys) [9]:

$$k(V) = \frac{k_e + V/V_D^I}{1 + V/V_D^I}, \qquad (2)$$

where k_e is the equilibrium partition coefficient given by the equilibrium phase diagram, while V_D^I is the speed of diffusion at the interface defined as $V_D^I = D_I/\lambda$. Here, D_I is the diffusion coefficient at the interface while λ is a characteristic distance, equal to the width of the solid–liquid interface. The quantitative analysis of such a function $k(V)$ in Eq. (2) according to CGM shows a reasonable agreement with the experimental data at small and moderate growth velocities of the solid. However, the experimental results suggest a complete solute trapping regime, i.e. $k(V) = 1$, occurs at a finite interface velocity, which cannot be predicted by CGM. In order to describe the increasing $k(V)$ up to $k(V) = 1$ at a finite interface velocity, both the speed of diffusion at the interface V_D^I and the speed of the atomic diffusion in the bulk V_D^B should be included in the model, as in LNM [11]. The LNM is based on a similar approach as the CGM, but makes use of a generalized Fick's law that accounts for the finite relaxation time of the diffusion flux into its steady state. As a result, the solute segregation coefficient in LNM is described by:

$$k(V) = \frac{\left[1 - (V/V_D^B)^2\right]k_e + V/V_D^I}{1 - (V/V_D^B)^2 + V/V_D^I}, \qquad V < V_D^B,$$
$$k(V) = 1, \qquad V \geqslant V_D^B. \qquad (3)$$

where V_D^B is the propagative speed of the front of solute diffusion profile.

Even though the analytical models may predict the velocity-dependent segregation coefficients, the evolution of the concentration or microstructure can be simulated using the phase-field method. For the past two decades, many attempts have been made to describe non-equilibrium effects in phase transformations [20–22] and, especially, in rapid

solidification [23,24]. In particular, the effects of solute trapping and solute drag have been treated by various phase-field models [14–20,25,26], which fall into two general classes. The first class is based on parabolic governing equations and, therefore, is termed the class of "parabolic phase-field models" [14–17,23,25,26]. The second class is described by hyperbolic-type partial differential equations, and is termed the class of "hyperbolic phase-field models" [18,19,21,24].

The simulated segregation coefficient $k(V)$ in the parabolic phase-field models increases monotonically and gradually as the interface velocity increases, which is consistent with the CGM model [8,9]. However, the complete solute trapping regime, i.e. $k(V) = 1$, cannot be reached by the parabolic phase-field models due to the infinite bulk diffusion speed V_D^B assumed in the model: only the diffusion speed within the interface, V_D^I, is considered in the diffusion equations for the parabolic models. In order to achieve the complete solute trapping regime and the transition to diffusionless solidification (observed in many experiments [6]), the hyperbolic phase-field model [18,19] has been developed by introducing a couple of partial differential equations of hyperbolic type into the original parabolic phase-field models, i.e. the Wheeler–Boettinger–McFadden (WBM) model [14] or the Echebarria–Folch–Karma–Plapp (EFKP) model [27]. By taking both speeds V_D^B and V_D^I into account, the hyperbolic phase-field model [19] predicts the complete solute trapping at the finite interface velocity with the exact value of V_D^B, which agrees well with the experimental data [28] and the atomistic simulations [29]. Considering the lack of experimental data (i.e. segregation coefficient) for most alloys, the simulation results given by the hyperbolic phase-field model can serve as a test as to whether reliable values for speeds V_D^B and V_D^I, and values for other material parameters are being used for the simulation. Note that, so far, the hyperbolic phase-field model can reproduce the complete solute trapping and experimental data with the nanometric width of the diffuse interface.

Very recently, a phase-field model with finite interface dissipation has been developed for the description of non-equilibrium phase transformations [30] on a mesoscopic scale. At this scale, the concentration field, which must be assumed continuous on the atomistic scale, is split into the phase concentrations defined for the individual bulk phases [3]. The solute redistribution at a moving phase boundary is then considered by a local redistribution flux between the phase concentration fields which overlap at the interface. The key feature of this model is that the two concentration fields are linked by a kinetic equation which describes the exchange of the components between the phases, instead of an equilibrium partitioning condition. To adjust the interface dissipation in this exchange, an interface permeability, P, was introduced into the model. For fast exchange (high permeability), the model recovers the phase-field model with equal diffusion potentials in coexisting phases [4,31,32]. In the case of small values of P, the non-equilibrium states of the diffuse interface can be modeled. The model has been applied to simulate the solute trapping in Si-9 at.% As alloy during rapid solid-

ification [30]. By adjusting the interface permeability P, and the numerical interface width η, an agreement with the experimental data [28] can be achieved with an interface width of 10^{-7} m. Even though the complete solute trapping regime cannot be obtained due to the nature of the parabolic model, the experimental data up to an interface velocity of $V = 2$ m s^{-1} can be predicted by the parabolic phase-field model with finite interface dissipation. In the present paper, we search for a relation between the interface permeability P and the mesoscopic interface width η, i.e. the width of the coarse graining. This relation is needed to perform multidimensional numerical simulations of solute trapping during rapid solidification on a mesoscopic scale.

Consequently, the models [19,30] are employed to study the solute-trapping effect in an alloy during rapid solidification. The solute segregation coefficient predicted by the hyperbolic model using the physical interface width is regarded as the standard "experimental data". By using the same material parameters, the interface width and the interface permeability are adjusted in the parabolic phase-field model with finite interface dissipation to fit the "experimental data" from the hyperbolic model. Several pairs of the interface width η and the interface permeability P are employed to describe the "experimental data".

The present paper is organized as follows. Both the hyperbolic model and the parabolic model with finite interface dissipation are formulated in Section 2. The parameter sets for both models and their equivalence are also introduced in that section. The different definitions of the solute segregation coefficient in both models are then given in Section 3. The numerical hints on simulation using both models are demonstrated in Section 4. In Section 5, the numerical results from both models are presented. The effects of the interface width η and interface permeability P on solute trapping are discussed. A summary of the conclusions is made in Section 6. Finally, in Appendix A, a diffusion equation with an anti-trapping current is derived in the form suggested for numerical calculations in the present work.

2. The models

2.1. The hyperbolic model

2.1.1. Model description

Consider the effect of solute atoms being trapped by rapid solidification in isothermal binary alloys at constant pressure. We assume that there is a binary system consisting of A-atoms (solvent) and B-atoms (solute) with the concentration c. Then the evolution of the system to equilibrium is described by the following equations of hyperbolic type [18,19,21]:

$$\tau_D \frac{\partial^2 c}{\partial t^2} + \frac{\partial c}{\partial t} = \vec{\nabla} \cdot \left[M_c \left(\frac{\partial^2 f}{\partial c^2} \vec{\nabla} c + \frac{\partial^2 f}{\partial c \partial \phi} \vec{\nabla} \phi \right) \right] - \vec{\nabla} \cdot \vec{j}_{AT}, \quad (4)$$

$$\tau_\phi \frac{\partial^2 \phi}{\partial t^2} + \frac{\partial \phi}{\partial t} = M_\phi \left(\varepsilon_\phi^2 \nabla^2 \phi - \frac{\partial f}{\partial \phi} \right), \quad (5)$$

where f is the local equilibrium free energy density, τ_D is the relaxation time for the diffusion flux, M_c is the mobility of the B-atoms, τ_ϕ is the timescale for the relaxation of the rate of change of the phase field $\partial \phi / \partial t$, and M_ϕ is the mobility of the phase field. Note especially that Eq. (4) includes the contribution $\vec{j}_{AT}$ which is the anti-trapping current through the diffuse interface of thickness δ suggested by Karma [33] in the following form:

$$\vec{j}_{AT} = -a\delta(1 - k_e)c_l e^{u(c,\phi)} \frac{\partial \phi}{\partial t} \frac{\vec{\nabla}\phi}{|\vec{\nabla}\phi|}, \quad (6)$$

where $c_l = c_s / k_e$ is the equilibrium concentration in the liquid at the solid–liquid interface, $u = \frac{v_m}{RT}(\mu - \mu_{eq})$ is the dimensionless difference of the chemical potentials, μ and μ_{eq} are the chemical potential and the equilibrium chemical potential, respectively, and $a = 1/(2\sqrt{2})$ is the parameter of the model for anti-trapping [33].

The local equilibrium free energy density f is chosen as the ideal solution of a dilute binary system [27]:

$$f(c, \phi) = f^A(T_A) - (T - T_A)s(\phi) + \epsilon(\phi)c + \frac{RT}{v_m}(c \ln c$$
$$- c) + Wg(\phi), \quad (7)$$

where $f^A(T)$ is the free energy density of a pure system consisting of the solvent (pure A-atoms), T_A is the solidification temperature of the solvent, R is the gas constant, v_m is the molar volume (assumed equal for A- and B-atoms), and W is the height of the energetic barrier which is modeled by the standard double-well potential:

$$g(\phi) = \phi^2(1 - \phi)^2. \quad (8)$$

To calculate the function $u(c, \phi)$ from Eq. (6), the chemical potential and equilibrium chemical potential, respectively, are given by:

$$\mu(c, \phi) = \frac{\partial f}{\partial c} = \epsilon(\phi) + \frac{RT}{v_m} \ln c, \quad (9)$$

$$\mu_{eq} = \epsilon_l + \frac{RT}{v_m} \ln c_l. \quad (10)$$

The entropy density $s(\phi)$ and the internal energy density $\epsilon(\phi)$ are derived using the dilute alloy approximation:

$$s(\phi) = \frac{s_s + s_l}{2} - \frac{L}{T_A}\left[\frac{1}{2} - p(\phi)\right], \quad (11)$$

$$\epsilon(\phi) = \frac{\epsilon_s + \epsilon_l}{2} - \frac{RT}{v_m}\left\{\ln[k_e + p(\phi)(1 - k_e)] - \frac{1}{2}\ln k_e\right\}, \quad (12)$$

where L is the latent heat of solidification, k_e is the equilibrium solute partition coefficient, and the indices l and s indicate the liquid and solid phases, respectively. The interpolation function $p(\phi)$ is taken to be:

$$p(\phi) = \phi^2(3 - 2\phi), \quad (13)$$

with

$$1 - p(\phi) = p(1 - \phi), \qquad \left.\frac{dp(\phi)}{d\phi}\right|_{\phi=0} = \left.\frac{dp(\phi)}{d\phi}\right|_{\phi=1} = 0. \quad (14)$$

These functions define the liquid state for $\phi = 1$ and the solid state for $\phi = 0$.

2.1.2. Model parameters

Now we choose the parameters of the phase field and solute diffusion for the hyperbolic model, Section 2.1.1. The present computations use the following model parameters (see Ref. [14] and the appendix in Ref. [32]): the gradient energy factor ε_ϕ^2, the energetic barrier height W, the capillary parameter d_0, and the mobility M_ϕ of the phase field expressed in terms of the surface energy σ, the interfacial width δ, and the phase-field diffusion parameter v:

$$\varepsilon_\phi^2 = 2\sigma\delta, \qquad W = \frac{9\sigma}{\delta},$$
$$d_0 = \frac{\sigma v_m}{RT_A}, \qquad M_\phi = \frac{v}{2\sigma\delta}. \tag{15}$$

Additionally, the atomic mobility is introduced as:

$$M_c(T, c, \phi) = \left(\frac{\partial^2 f}{\partial c^2}\right)^{-1} D(\phi). \tag{16}$$

Note that the phase-field mobility from Eq. (15) is assumed to be positive at the positive phase-field diffusivity $v > 0$ and the atomic mobility (16) is positive at $\partial^2 f / \partial c^2 > 0$. This guarantees a monotonic decrease in the free energy over time for the solidifying binary system [34].

The equilibrium partition coefficient k_e can be expressed through the energetic barrier between coexisting phases as follows. In equilibrium, the chemical potentials of the liquid and solid phases, $\mu_l = \partial f_l / \partial c_l = \epsilon_l + (RT/v_m)\ln c_l$ and $\mu_s = \partial f_s / \partial c_s = \epsilon_s + (RT/v_m)\ln c_s$ give the equality:

$$\epsilon_l + \frac{RT}{v_m}\ln c_l = \epsilon_s + \frac{RT}{v_m}\ln c_s, \tag{17}$$

where ϵ_l and ϵ_s present the internal energy density of the liquid and solid, respectively. From Eq. (17) the definition of the solute segregation coefficient in equilibrium directly follows as:

$$k_e \equiv \frac{c_s}{c_l} = \exp\left(-\frac{v_m}{RT}\Delta\epsilon\right), \tag{18}$$

where

$$\Delta\epsilon = \epsilon_s - \epsilon_l, \tag{19}$$

is the difference between internal energy densities of phases.

In addition to the parameters used usually for the systems evolving around equilibrium, the present problem of a fast propagating interface includes four additional kinetic parameters, given in Table 1. These parameters present the characteristic speeds V_D^I and V_D^B for the solute diffusion and characteristic speeds V_ϕ^I and V_ϕ^B for the interface propagation. They are defined by the thickness δ of the interface and the relaxation times of the solute diffusion and phase fields to local equilibrium.

2.1.3. Traveling wave solution

The properties and features of the hyperbolic equations for diffuse interface models were discussed and analyzed in

Refs. [18,19,21]. Here we demonstrate the peculiarities of the hyperbolic phase-field equation in an example of its traveling wave solution.

The phase-field Eq. (5) can be rewritten in the form:

$$\tau_\phi \frac{\partial^2 \phi}{\partial t^2} + \frac{\partial \phi}{\partial t} = v\left(\nabla^2 \phi - \frac{1}{2\sigma\delta}\frac{\partial f}{\partial \phi}\right), \tag{20}$$

where the relation among the coefficients (15) has been used. Taking the derivative from the free energy density (7) as $\partial f(c,\phi)/\partial \phi = -(T - T_A)ds/d\phi + cd\epsilon/d\phi + Wdg/d\phi$ and using Eq. (8) and Eqs. (11)–(13), one can rewrite Eq. (20) in the following form:

$$\tau_\phi \frac{\partial^2 \phi}{\partial t^2} + \frac{\partial \phi}{\partial t} = v\left\{\left[\nabla^2 \phi + \frac{18}{\delta^2}\phi(1-\phi)(\phi - \frac{1}{2})\right] + \frac{\Lambda^*(T,c,\phi)}{\sigma\delta}3\phi(1-\phi)\right\}, \tag{21}$$

where the function

$$\Lambda^*(T,c,\phi) = \frac{RT}{v_m} \cdot \frac{(1-k_e)c}{k_e + (1-k_e)p(\phi)} + \frac{T - T_A}{T_A}L$$
$$= -\frac{RT}{v_m}\left(\Theta(\phi)c + \frac{1-k_e}{m_e}(T - T_A)\right)$$
$$= \frac{RT}{v_m}\Lambda(T,c,\phi) \tag{22}$$

includes the contributions

$$\Theta(\phi) = -\frac{1-k_e}{k_e + (1-k_e)p(\phi)}, \tag{23}$$

$$\Lambda(T,c,\phi) = \frac{(1-k_e)c}{k_e + (1-k_e)p(\phi)} - \frac{1-k_e}{m_e}(T - T_A), \tag{24}$$

which characterize the driving forces for the diffusion and the phase transformation, respectively. All parameters are described in Table 1.

We obtain a traveling wave solution at a given constant driving force with the following average value in the steady state:

$$\Delta G = -\langle \Lambda^*(T,c,\phi)\rangle, \tag{25}$$

where the average $\langle \cdots \rangle$ is taken in the normal direction over the interface, as described in Ref. [32]. The equilibrium condition $\Delta G = 0$ gives for Eqs. (22) and (25) the equilibrium value of k_e which can be used for the definition of the non-equilibrium solute segregation function $k(V)$ in full analogy with the analysis of [19]. A one-dimensional solution of Eq. (21) in the form of a traveling wave, $\phi = \phi(z)$ with $z = x - Vt$, can be found in the reference frame moving with the constant velocity V. Then, Eq. (21) becomes:

$$\left(1 - \frac{\tau_\phi V^2}{v}\right)\frac{d^2\phi}{dz^2} + \frac{V}{v}\frac{d\phi}{dz} + \frac{18}{\delta^2}\phi(1-\phi)\left(\phi - \frac{1}{2}\right)$$
$$- 3\phi(1-\phi)\frac{\Delta G}{\sigma\delta} = 0. \tag{26}$$

The solution of Eq. (26) has the same form as for the phase-field model utilizing a double-well potential [19]:

Table 1
Physical parameters of the Si-0.25 at.% As alloy used for phase-field modeling.

Parameter	Value	Ref.
Melting temperature of Si, T_A	1685 K	[35]
Liquidus line slope, m_e	-400 at.%$^{-1}$	[17]
Solute partitioning coefficient, k_e	0.3	[28]
Molar volume, v_m	1.2×10^{-5} m^3 mol^{-1}	[17]
Diffusion coefficient in liquid, D_L	1.5×10^{-9} m^2 s^{-1}	[28]
Diffusion coefficient in solid, D_S	3×10^{-13} m^2 s^{-1}	[28]
Surface energy, σ	0.477 J m^{-2}	[35]
Phase-field diffusion parameter, v	1.57×10^{-8} m^2 s^{-1}	[19]
Interfacial thickness, $\delta = \delta_{atom}$	1.875×10^{-9} m	[18]
Interface mobility, $M_\phi\|_{\delta=\delta_{atom}}$	8.777 m^3 J^{-1} s^{-1}	Present work
Mobility of the "thick" interface, $M'_\phi\|_{\delta=10\delta_{atom}}$	87.77×10^{-3} m^3 J^{-1} s^{-1}	Present work
Relaxation time for the phase-field rate, τ_ϕ	1.0×10^{-11} s	[18]
Relaxation time for the diffusion flux, τ_D	2.4×10^{-10} s	[19]
Scale speed for the ϕ-field, $V_\phi^I = v/\delta$	8.37 m s^{-1}	[19]
Maximum speed for ϕ propagation, $V_\phi^B = (v/\tau_\phi)^{1/2}$	39.6 m s^{-1}	[19]
Solute diffusion speed within the interface, $V_D^I = D_L/\delta$	0.8 m s^{-1}	[13]
Solute diffusion speed in the bulk, $V_D^B = (D_L/\tau_D)^{1/2}$	2.5 m s^{-1}	[13]

$$\phi = \frac{1}{2}\left[1 + \tanh\left(\frac{z}{l}\right)\right], \tag{27}$$

where l is the the correlation length of the phase field. Differentiating the solution (27) with respect to z two times, $d\phi/dz = 2\phi(1-\phi)/l$ and $d^2\phi/dz^2 = 8\phi(1-\phi)(1-\phi/2)/l^2$, we substitute the results into Eq. (26). Having equating the coefficients for ϕ of the same order to zero, one can finally obtain:

– the velocity-corrected correlation length

$$l = \frac{2\delta}{3}\sqrt{1 - \frac{\tau_\phi V^2}{v}}, \tag{28}$$

– the diffuse interface velocity

$$V = \frac{v\Delta G}{\sigma}\sqrt{1 - \frac{\tau_\phi V^2}{v}}, \tag{29}$$

which, for real values of V, is true with the following inequality $|V| < \sqrt{v/\tau_\phi}$. This inequality recognizes the cases of solidification $0 < V < \sqrt{v/\tau_\phi}$ and melting $-\sqrt{v/\tau_\phi} < V < 0$. As a result, it follows from Eq. (28) that the correlation length l decreases with an increase in the interface velocity $V \to \sqrt{v/\tau_\phi}$.

Assuming in the following analysis the theoretical velocity, $V = V_{th}$, Eqs. (28) and (29) are described by:

$$V_{th} = \frac{v\Delta G}{\sqrt{\sigma^2 + \tau_\phi v\Delta G^2}}, \qquad l = \frac{2\delta\sigma}{3\sqrt{\sigma^2 + \tau_\phi v\Delta G^2}}, \tag{30}$$

from which two limiting cases can be outlined. First, a maximum speed V_{max} with which the disturbances of the phase field can propagate and the effective interface width on the front of these disturbances are obtained at the infinite driving force, $\Delta G \to \infty$:

$$V_{th}|_{\Delta G\to\infty} \equiv V_{max} = \sqrt{\frac{v}{\tau_\phi}}, \qquad l|_{V\to V_{max}} \to 0. \tag{31}$$

The limit (31) is absent in the parabolic model in which disturbances of the phase field propagate with infinite speed, i.e. $V_{max} \to \infty$. Second, the diffuse interface velocity and the correlation length in a system described by the parabolic equation are obtained in the local equilibrium limit, $\tau_\phi \to 0$:

$$V_{th}|_{\tau_\phi=0} = \frac{v}{\sigma}\Delta G, \qquad l|_{\tau_\phi=0} = 2\delta/3. \tag{32}$$

As a result, the kink solution, Eq. (27), of the hyperbolic phase-field Eq. (26) exhibits the following outcomes. (i) The diffuse interface velocity is limited by the finite speed for disturbance propagation, $|V| < \sqrt{v/\tau_\phi} = V_{max}$ (see Eqs. (29) and (31)). (ii) The phase field disturbance propagates with the sharp front, $l = 0$, having the finite speed, V_{max} (see Eqs. (28) and (31)). (iii) In the local equilibrium system described by the parabolic phase-field equation (see Eq. (21) with $\tau_\phi = 0$), the diffuse interface moves with the correlation length proportional to the interface thickness, $l = 2\delta/3$, and its steady-state velocity is linearly proportional to the driving force, $V \propto \Delta G$ (see Eq. (32)).

To predict the diffuse interface velocity independently from the analytical predictions, we carried out some numerical modeling. By solving one-dimensional non-stationary Eq. (21) numerically, we obtained the profile for the phase field and its steady-state velocity V. The numerical calculations were carried out using a non-stationary explicit finite-difference scheme with four time layers. Moving-frame boundary conditions were used. Starting from some initial configuration for the phase-field profile, the evolution of the profile was calculated up to the point at which a steady state with a constant velocity was achieved. We assume that $\tau_\phi = 10^{-11}$ s, $v = \tau_\phi V_{max}^2 = 9 \times 10^{-9}$ m^2 s^{-1}. Fig. 1 compares the results of the numerical calculations

for the interface velocity with the theoretical interface velocity. It can be seen that the existence of the analytical solution (30) is confirmed by the numerical solution of the one-dimensional non-stationary Eq. (21) with good agreement.

2.2. The parabolic model with finite interface dissipation

2.2.1. Model description

Following our recent paper [30], we treat two distinct phase-field variables ϕ_α and ϕ_β, which are connected by $\phi_\beta = 1 - \phi_\alpha$ for a dual-phase alloy. This difference in notation indicates the use of a double-obstacle potential in the free energy for computational reasons. Using the double-obstacle potential does not hamper the comparability of the results of the hyperbolic model, because we use the same physical entities for the material properties (see below). The interface thickness will now be treated on a mesoscopic scale with width η to be distinguished from the hyperbolic model, where the interface width δ was taken as a physical entity. For our binary alloy exhibiting a single $\alpha - \beta$ transition (two components, two phases), the total free energy F in any arbitrary thermodynamic state can be split into the interfacial part f^{intf} and the chemical part f^{chem}:

$$F = \int_\Omega \{f^{intf} + f^{chem}\}, \tag{33}$$

$$f^{intf} = \frac{4\sigma_{\alpha\beta}}{\eta} \left\{ -\frac{\eta^2}{\pi^2} \nabla \phi_\alpha \cdot \nabla \phi_\beta + \phi_\alpha \phi_\beta \right\}, \tag{34}$$

$$f^{chem} = \phi_\alpha f_\alpha(c_\alpha) + \phi_\beta f_\beta(c_\beta) + \lambda \{c - (\phi_\alpha c_\alpha + \phi_\beta c_\beta)\}, \tag{35}$$

where η is the interface width, $\sigma_{\alpha\beta}$ is the interfacial free energy, ϕ_α is the phase field for phase α that varies between 0 (not phase α) and 1 (phase α), and its complement $\phi_\beta = 1 - \phi_\alpha$. f_α and f_β are the volume free energy of the α and β phases, which depend on the respective phase concentrations, c_α and c_β. The phase concentrations, c_α and c_β, are related with the overall concentration via the mixture rule

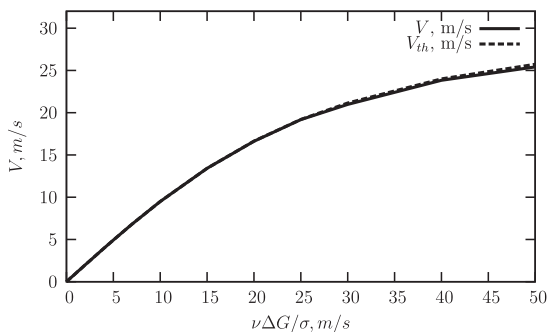$$c = \phi_\alpha c_\alpha + \phi_\beta c_\beta. \tag{36}$$

Fig. 1. Comparison of the numerically calculated interface velocity V with the theoretically obtained interface velocity V_{th}, Eq. (30).

To ensure solute conservation, the Lagrange multiplier λ is introduced in the chemical energy density f^{chem}, expressed as:

$$\lambda = \phi_\alpha \tilde{\mu}_\alpha + \phi_\beta \tilde{\mu}_\beta - \frac{\frac{\partial \phi_\alpha}{\partial t} c_\alpha + \frac{\partial \phi_\beta}{\partial t} c_\beta}{P}. \tag{37}$$

Here, $\tilde{\mu}_\alpha$ and $\tilde{\mu}_\beta$ are the diffusion potentials of the α and β phases, and are defined as $\partial f_\alpha / \partial c_\alpha$ and $\partial f_\beta / \partial c_\beta$, respectively. $\partial \phi_\alpha / \partial t$ and $\partial \phi_\beta / \partial t$ denote the temporal phase changes of the α and β phases, respectively. P is the so-called interface permeability against redistribution fluxes. In fact, P is the rate constant controlling the interface dissipation, and can be estimated as:

$$P = f(\eta) \frac{M^{inter}}{\delta_{atom}}, \tag{38}$$

where δ_{atom} is the atomistic interface width as given in Table 1. $M^{inter} = \phi_\alpha M_\alpha + \phi_\beta M_\beta$ is the atomic mobility over the interface as a mixture from the chemical mobility in α and β, respectively. Hence it is comparable to $M_c(T, c, \phi)$ in the hyperbolic model Eq. (16). $f(\eta)$ is a function of the numerical interface width η with the dimension [m^{-1}]. A first approximation of $f(\eta)$ has been set to be $8/\eta$ in our previous paper [30]. In fact, the relation between P and η is to be determined in the present paper by acquiring a series of optimal P and η with which the "experimental data" can be well reproduced.

The role of the interface permeability can be clarified in the case of an atomistic interface width $\eta \approx \delta_{atom}$ as a kinetic correction if the solute does not instantaneously follow a phase change. This leads to a kinetic correction of the generalized chemical potential λ in Eq. (37) proportional to $\partial \phi / \partial t$. In the case of a mesoscopic interface $\eta \gg \delta_{atom}$, the correction can be derived from a coarse-graining procedure applied to the diffusion equation:

$$\frac{\partial c}{\partial t} = \nabla \cdot \left(M_c \nabla \frac{\partial f}{\partial c} \right) = \nabla \cdot (M_c \nabla \mu), \tag{39}$$

where M_c is the chemical mobility and f the free energy density, e.g. taken from Eq. (7) in the limit $\eta = \delta_{atom}$ and μ is the chemical potential. In fact, Eq. (39) is equivalent to the divergence of flux terms $\vec{\nabla} \cdot \left[M_c \left(\frac{\partial^2 f}{\partial c^2} \vec{\nabla} c + \frac{\partial^2 f}{\partial c \partial \phi} \vec{\nabla} \phi \right) \right]$ in the hyperbolic model (see Eq. (4)). In a one-dimensional domain normal to the interface we perform the Fourier transform (where M_c is taken as a constant):

$$\mu(\vec{x}) = \int \mu(\vec{k}) e^{-2\pi i \vec{k}\vec{x}} d\vec{k}; \quad \mu(\vec{k}) = \int \mu(\vec{x}) e^{2\pi i \vec{k}\vec{x}} d\vec{x};$$

$$\frac{\partial c(\vec{x})}{\partial t} = -4\pi^2 M \int k^2 \mu(\vec{k}) e^{-2\pi i \vec{k}\vec{x}} d\vec{k}. \tag{40}$$

Now we split the Fourier modes into long-range and short-range fluctuations with a cut-off wave vector $k_0 = 1/\eta$. We will be interested in keeping only the long-wavelength modes with $|k| < k_0$, where η sets the minimum resolution on the mesoscopic scale. This leads to the coarse-grained equation in each phase α and β which has a non-zero value of the phase-field variable $\phi_\alpha \neq 0$ or $\phi_\beta \neq 0$ in the domain Ω_α and Ω_β, respectively,

$$\frac{\partial c_\alpha(\vec{x})}{\partial t} = -4\pi^2 M \int_{|\vec{k}|<k_0} k^2 \mu(\vec{k}) e^{-2\pi i \vec{k} \vec{x}} d\vec{k} + P(\mu_\beta - \mu_\alpha);$$
$$\vec{x} \in \Omega_\alpha \tag{41}$$

$$\frac{\partial c_\beta(\vec{x})}{\partial t} = -4\pi^2 M \int_{|\vec{k}|<k_0} k^2 \mu(\vec{k}) e^{-2\pi i \vec{k} \vec{x}} d\vec{k} + P(\mu_\alpha - \mu_\beta);$$
$$\vec{x} \in \Omega_\beta. \tag{42}$$

and

$$P = -\frac{4\pi^2 M}{(\mu_\alpha - \mu_\beta)} \int_{|\vec{k}| \geqslant k_0} k^2 \mu(\vec{k}) e^{-2\pi i \vec{k} \vec{x}} d\vec{k}. \tag{43}$$

There is no longer a direct diffusion flux between the phases. This is now replaced by the redistribution flux $P(\mu_\beta - \mu_\alpha)$, which is of course symmetric between the phases.[2] The long-range fluctuations describe the smooth variations in the bulk phases, but not the jump of the chemical potential over the interface between the phases. Therefore Eqs. (41) and (42) are restricted to phase α and phase β, respectively. The last term in Eqs. (41) and (42) describes the redistribution flux through the interface between the different phases which is formally defined as the sum of all short-wavelength fluctuations. The kinetic parameter P will be called the "interface permeability" (see Ref. [30]). Transforming back to real space, we have:

$$\frac{\partial c_\alpha}{\partial t} = \nabla \cdot (M \nabla \mu_\alpha) + P(\mu_\beta - \mu_\alpha), \tag{44}$$

$$\frac{\partial c_\beta}{\partial t} = \nabla \cdot (M \nabla \mu_\beta) + P(\mu_\alpha - \mu_\beta). \tag{45}$$

In the case of a phase transformation, there will be in addition a correction to take into account of mass conservation during the transformation. This correction is formally derived from a Lagrange condition (37), as explained in detail in Ref. [30]. The obtained evolution equations for the phase concentrations c_α and c_β based upon the free energy functional (33) and (34) according to Ref. [30] are:

$$\phi_\alpha \frac{\partial c_\alpha}{\partial t} = \vec{\nabla} \cdot (\phi_\alpha D_\alpha \vec{\nabla} c_\alpha) + P \phi_\alpha \phi_\beta (\tilde{\mu}_\beta - \tilde{\mu}_\alpha) + \phi_\alpha \frac{\partial \phi_\alpha}{\partial t} \times (c_\beta - c_\alpha), \tag{46}$$

$$\phi_\beta \frac{\partial c_\beta}{\partial t} = \vec{\nabla} \cdot (\phi_\beta D_\beta \vec{\nabla} c_\beta) + P \phi_\alpha \phi_\beta (\tilde{\mu}_\alpha - \tilde{\mu}_\beta) + \phi_\beta \frac{\partial \phi_\beta}{\partial t} \times (c_\alpha - c_\beta). \tag{47}$$

Here, D_α and D_β are the chemical diffusivities of the α and β phases, respectively. They can be either directly obtained from the experimental measurements or calculated from the atomic mobilities. The relation between the chemical

diffusivities and the atomic mobilities can be found in our recent paper [30,36].

The evolution equation for the phase field ϕ_α is:

$$\frac{\partial \phi_\alpha}{\partial t} = K \left\{ \sigma_{\alpha\beta} \left[\nabla^2 \phi_\alpha + \frac{\pi^2}{\eta^2} \left(\phi_\alpha - \frac{1}{2} \right) \right] + \frac{\pi}{\eta} \sqrt{\phi_\alpha \phi_\beta} \Delta g_{\alpha\beta}^{phi} \right\}. \tag{48}$$

K introduced in Eq. (48) is the modified interface mobility given by:

$$K = \frac{8P\eta\mu_{\alpha\beta}}{8P\eta + \mu_{\alpha\beta}\pi^2(c_\alpha - c_\beta)^2}, \tag{49}$$

with the physical interface mobility $\mu_{\alpha\beta}$ between the α and β phases, and $\Delta g_{\alpha\beta}^{phi}$ the driving force for the phase field, defined by:

$$\Delta g_{\alpha\beta}^{phi} = f_\beta - f_\alpha - (\phi_\alpha \tilde{\mu}_\alpha + \phi_\beta \tilde{\mu}_\beta)(c_\beta - c_\alpha). \tag{50}$$

Summing Eqs. (46) and (47) gives the standard evolution equation of the overall concentration, $\partial c / \partial t = \vec{\nabla} \cdot (\phi_\alpha D_\alpha \vec{\nabla} c_\alpha) + \vec{\nabla} \cdot (\phi_\beta D_\beta \vec{\nabla} c_\beta)$, where we have used the fact that $\partial \phi_\alpha / \partial t = -\partial \phi_\beta / \partial t$. The non-trivial point in solving Eqs. (46) and (47) separately is that this obviates the need to employ an extra condition to fix the concentrations for each phase. Instead, we can use the separate concentration evolution equations of each phase for the iteration, which is applicable for arbitrary initial conditions.

2.2.2. Model parameters

The liquid–solid transition during rapid solidification is the present target, and α and β in the parabolic model with finite interface dissipation described in Section 2.2.1 are thus the liquid and solid phases. In order to make a direct comparison between the simulation results from the two models, the same physical parameters are used, including the interfacial energy, diffusivity, thermodynamic properties and interface mobility.

The diffusivities D_L, D_S, interfacial energy, σ_{LS} used in Eqs. (46)–(48), are simply taken from Table 1. Based on the phase equilibria information presented in Table 1, i.e. liquidus slope m_e, equilibrium partitioning coefficient k_e, and melting temperature T_A for pure Si, the corresponding free energy densities of liquid and solid phases for constructing the same linear Si–As system are listed as follows [18,30,36]:

$$f_L = \frac{RT}{v_m} \{ c_L \ln(c_L) + (1 - c_L) \ln(1 - c_L) \}, \tag{51}$$

$$f_S = \frac{RT}{v_m} \left\{ c_S \ln(c_S) + (1 - c_S) \ln(1 - c_S) - c_S \ln(k_e) + (1 - c_S) \ln \left[\frac{1 + (T_A - T)/m_e}{1 + k_e(T_A - T)/m_e} \right] \right\}. \tag{52}$$

Here, R is the ideal gas constant, T is the simulation temperature, while c_L and c_S are the concentrations of the liquid and the solid. V_m is the molar volume, which is also taken from Table 1.

---

[2] Since the spatial information about the phases is lost by integration of the short-wavelength fluctuations, one has to recapture this information by the sign of the difference in the chemical potentials.
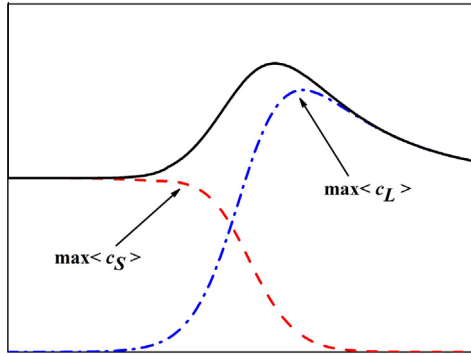
Fig. 2. The definition of solute segregation coefficient $k(V)$ by the ratio (54) of maximum concentrations in phases. The solid line shows the total concentration c obtained from the hyperbolic model in Section 2.1. The dashed curve is given by Eq. (55) and the dashed-dotted curve is given by Eq. (56).

The interface mobility μ_{LS}, which is used in the parabolic phase-field model, is related to the surface energy σ and the phase-field diffusion parameter v by:

$$\mu_{LS} = \frac{v}{\sigma}. \tag{53}$$

The mobility (53) can be interpreted as the kinetic coefficient in Eq. (32) for the "interface velocity–driving force" relationship.

3. Definitions of the solute segregation coefficient

3.1. The segregation coefficient in the hyperbolic model

To obtain the solute segregation coefficient (1) quantitatively, one has to give a definition for it on the diffuse interface, which requires special consideration. For instance, the segregation coefficient has been defined by the values of the concentrations at the ends of the diffuse interface [18]:

$$k(V) = \frac{c_S \equiv c(\phi \to 0)}{c_L \equiv c(\phi \to 1)}.$$

This definition does indeed give the transition to diffusionless solidification at a finite interface velocity V that qualitatively agrees with numerous experimental data. However this definition predicts a complete solute trapping at the interface velocity smaller than the solute diffusion speed in the bulk liquid, $V < V_D^B$, which contradicts its own definition of the transition to diffusionless solidification (see the results and discussion in Ref. [37]). Therefore, a segregation coefficient $k(V)$ can be introduced such that the concentrations at the diffuse interface become equal to their equilibrium values given by the solution of the phase-field equations in equilibrium, and these are approximated by the non-equilibrium stationary regime of solidification [19]. Then the coefficient $k(V)$ is defined as the ratio of the maximum concentration in the solid and the maximum concentration in the liquid (see Fig. 2):

$$k(V) = \frac{\max\langle c_S \rangle}{\max\langle c_L \rangle}, \tag{54}$$

where

$$\langle c_S(x) \rangle = [1 - h(p(\phi, V))]c(x), \tag{55}$$

$$\langle c_L(x) \rangle = h[p(\phi, V)]c(x), \tag{56}$$

with

$$h(p, V) = \frac{p(\phi)}{k(V) + [1 - k(V)]p(\phi)}, \tag{57}$$

and $p(\phi)$ given by Eq. (13) such that

$$c(x) = \langle c_S(x) \rangle + \langle c_L(x) \rangle. \tag{58}$$

Eqs. (54)–(57) give the solution of the phase-field equations in equilibrium, i.e. at $V = 0$, and give the equilibrium value for the solute segregation coefficient $k(V = 0) = k_e$. From the definition (58) it follows that $\langle c_S(x) \rangle$ and $\langle c_L(x) \rangle$ can be interpreted as the concentration fractions in solid and liquid, respectively.

3.2. The segregation coefficient in the parabolic phase-field model with finite interface dissipation

In the present parabolic model we assume that the individual phase concentrations are known and each position over the interface can be assumed to be a sharp interface. Then, we use the following definition for the solute segregation coefficient [30]:

$$k(V) = \frac{\text{far} - \text{field concentration}}{\text{maximum of the liquid concentration}}$$
$$= \frac{c_S}{\max[c_L]} = \frac{c_S}{c_L(\phi = 0.9999)}. \tag{59}$$

Here, the far-field concentration in the liquid is equal to the concentration in the bulk solid under steady-state conditions, while the maximum of the liquid concentration over the interface here is at the position adjacent to the solid bulk region. For simplicity, we assume that the maximum liquid concentration is the liquid concentration at $\phi = 0.9999$. These concentrations are schematically demonstrated in a typical concentration profile across a moving solid–liquid interface during rapid solidification, as shown in Fig. 3. In fact, this liquid concentration, $c_L(\phi = 0.9999)$, approaches its equilibrium value from the phase diagram during slow solidification. By comparing Eq. (59) with Eq. (1), it can be seen that this definition of the solute segregation coefficient $k(V)$ can be nicely reduced to the standard definition in terms of the sharp interface assumption. Therefore, the definition (59) is used to calculate the solute segregation coefficient for the simulation with the parabolic phase-field model with finite interface dissipation.

4. Numerical solution

The binary alloy Si-0.25 at.% As during rapid solidification is chosen as the target alloy for both phase-field
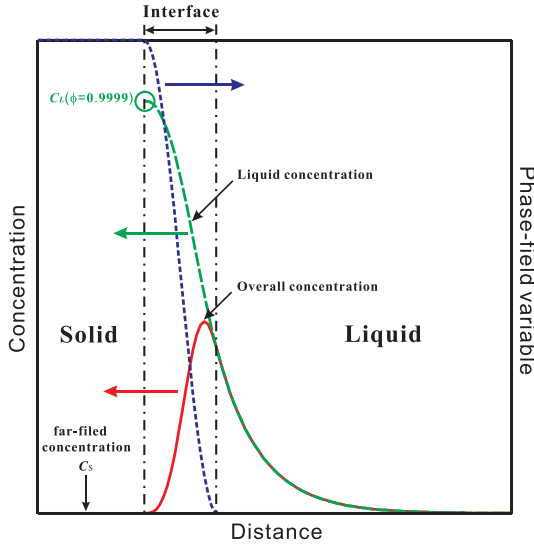
Fig. 3. Concentration profile across a moving solid–liquid interface during rapid solidification according to the parabolic phase-field model with finite interface dissipation.

models. The rapid solidification is initiated by a large difference of the free energy between the stable solid and the metastable liquid that in general occurs when a system is quenched far below the liquidus temperature [6].

4.1. The hyperbolic model

The effect of solute trapping is analyzed in one spatial dimension with a planar interface using the model parameters (15) and (16) and the values of Table 1. In the reference frame, $x \rightarrow (x - Vt)/\delta$ and $t \rightarrow tv/\delta^2$, moving with the constant interface velocity V, the governing Eqs. (4) and (5) can be written in dimensionless form for the concentration field and for the phase field (see Appendix A):

$$-\frac{V}{V_D^I}\frac{dc}{dx} = \frac{d}{dx}\left[\left(\widehat{D}(\phi) - \frac{V^2}{\left(V_D^B\right)^2}\right)\frac{dc}{dx}\right]$$
$$+ \frac{d}{dx}\left(\widehat{D}(\phi)c\Theta(\phi)\frac{dp(\phi)}{d\phi}\frac{d\phi}{dx}\right) + a(\phi)$$
$$\times \frac{V}{V_D^I}c\Theta(\phi)\frac{d\phi}{dx}, \quad (60)$$

$$-\frac{V}{V_\phi^I}\frac{d\phi}{dx} = \left(1 - \frac{V^2}{\left(V_\phi^B\right)^2}\right)\frac{d^2\phi}{dx^2} - \frac{9}{2}\frac{dg(\phi)}{d\phi} + \frac{1}{2}\frac{\delta}{d_0}$$
$$\times \frac{T}{T_A}\Lambda(T, C, \phi)\frac{dp(\phi)}{d\phi}, \quad (61)$$

where the dimensionless diffusion coefficient is

$$\widehat{D}(\phi) = D(\phi)/D_L = D_S/D_L + p(\phi)(1 - D_S/D_L), \quad (62)$$

and the driving forces $\Theta(\phi)$ and $\Lambda(T,c,\phi)$ are given by Eqs. (23) and (24), respectively. Note that all above material parameters are described in Table 1.

The last terms in Eqs. (60) and (61) depend on the ratio δ/d_0. Therefore, to have scale invariance, the change in the

interface thickness δ should lead to a change in the capillary length of $d_0 \propto \sigma$. As a result, we need to change the surface tension σ, which becomes physically unrealistic. To avoid this problem, we define d_0 by the phase-field mobility M_ϕ as [14,18,19]

$$d_0 = \frac{v_m}{RT} \cdot \frac{v}{2\delta M_\phi}. \quad (63)$$

Using this relation in the ratio δ/d_0, one gets:

$$\frac{\delta}{d_0} = 2\frac{RT}{v_m} \cdot \frac{\delta^2 M_\phi}{v} \equiv const., \quad (64)$$

which should be a constant equal to the ratio δ_{atom}/d_0 from Table 1. The phase-field diffusion v is defined by the kinetic coefficient of the crystal growth and, therefore, it has a physical meaning. To obtain a constant-valued relation (64), it is necessary to take the dependence of the phase-field mobility on the interface thickness to be $M_\phi \propto 1/\delta^2$. As a result, an increase of interface thickness by one order of magnitude leads to a decrease of the phase-field mobility by two orders, i.e.

$$M_\phi = 8.78 \quad \frac{m^3}{J\,s}, \qquad \delta = \delta_{atom},$$

$$M_\phi' = 8.78 \times 10^{-2} \quad \frac{m^3}{J\,s}, \qquad \delta = 10 \cdot \delta_{atom}.$$

We will use this result in the calculations for the cases of nanoscaled (atomistic) interface with the thickness $\delta = \delta_{atom}$ and the increased interface with the thickness $\delta = 10 \cdot \delta_{atom}$ (see Table 1).

4.2. The parabolic model with finite interface dissipation

The simulations using the parabolic model with finite interface dissipation are performed under isothermal conditions with different temperatures, which are below the solidus temperature of the Si-0.25 at.% As alloy. With these settings, the steady-state growth can be achieved during the simulation. The typical steady-state concentration and phase-field profiles across a moving solid–liquid interface during rapid solidification according to the parabolic phase-field model with finite interface dissipation has already been shown in Fig. 3. When decreasing the simulation temperature, the driving force becomes larger, resulting in an increase in the interface velocity.

One-dimensional phase-field simulations are performed by simultaneously solving the phase concentration evolution Eqs. (46) and (47) and the phase-field evolution Eq. (48) using the explicit finite-difference scheme. The total simulation size is large enough to keep a length of 10 times the diffusion length of the liquid profile when a lower interface velocity is used. 20 grid points are equally distributed over the interface during the simulation. The left and right boundaries for the phase field are set as insulation conditions. As for the concentrations, an insulation condition is employed for the left boundary, while the concentration at the right boundary is fixed at the initial alloy concentration, i.e.

Si-0.25 at.% As. A moving frame is used to determine the interface velocity. The thermophysical parameters, such as the interface energy, interface mobility, diffusivities and thermodynamic parameters, are taken from Table 1, as described in Section 2.2.2. By changing the simulation temperature, the interface velocity and segregation coefficient vary simultaneously. One thus obtains a unique relation between the interface velocity and the segregation coefficient.

In fact, the interface width η and interface permeability P are also adjusted to fit the "experimental data" from the hyperbolic model, as demonstrated in our previous paper [30]. The interface permeability P corresponding to the thermophysical parameters in Table 1 and the atomistic interface width η_{atom} (equal to δ_{atom} in the hyperbolic model) is calculated to be 2×10^3 cm^3 J^{-1} s^{-1} using Eq. (34) in Ref. [30]. This P value (2×10^3 cm^3 J^{-1} s^{-1}) in fact is an upper limit, above which there is a fast relaxation between the liquid and solid. Thus, a decrease in P leads to a decrease in the relaxation between the atoms in the liquid and the solid phases, and then the solute trapping will be enhanced.

5. Results and discussion

The solution of the hyperbolic model described by Eqs. (60) and (24) was done by the method developed in Refs. [18,19]. The kinetics and solute trapping for the cases of a nanoscaled (atomistic) interface width δ_{atom} and a wide interface $10\delta_{atom}$ were analyzed for rapid solidification of Si-0.25 at.% As alloy. The simulated results from the hyperbolic model are presented in Figs. 4 and 5.

Fig. 4 exhibits the kinetics of interface motion. It can be seen that the interface without an anti-trapping current moves slowly in comparison with the interface having an anti-trapping current. Therefore, the anti-trapping current rejects the solute from the wide interface to make the interface faster and much more mobile.

Fig. 5 shows the predictions of the hyperbolic EFKP model for complete solute trapping at $V = V_D^B$ for atomistic-scale interface width (1.875 nm). In addition, the model predicts a complete solute trapping at a smaller velocity $V < V_D^B$ for larger interface widths, as shown in Fig. 5b with and without an anti-trapping current. This occurs due to the effect of abnormal solute trapping by the broad diffuse interface having a purely numerical origin [33,27]. The numerical solute trapping effect is something additional, on top of the physically reasonable solute trapping, and gives rise to a complete solute trapping at a smaller interface velocity. For an interface width equal to 18.75 nm (i.e. $10\delta_{atom}$) with an anti-trapping current, the solute segregation coefficient behaves similarly to the case with an interface width equal to 1.875 nm only at low interface velocities (at $V < 0.1$ m s^{-1} in Fig. 5a). At high interface velocities the curves diverge. Therefore, the anti-trapping current (6) does not compensate for the numerical solute trapping for the whole range of velocity in modeling

with the wide diffuse interface. The current (6) compensates for the numerical solute trapping only for small interface velocities V (see Fig. 5b).

As stated in Section 1, the simulated results with δ_{atom} due to the hyperbolic phase-field model are regarded as the standard "experimental data". To fit the "experimental" segregation coefficients shown in Fig. 5, we investigate the dependence of the interface permeability P and the interface width η on the velocity-dependent solute segregation coefficient $k(V)$ in the parabolic model. Thus, three sets of $\eta - P$ values are employed in this paper, namely $\eta_{atom} - 2000$ cm^3 J^{-1} s^{-1}, $\eta_{atom} - 200$ cm^3 J^{-1} s^{-1}, and $10\eta_{atom} - 200$ cm^3 J^{-1} s^{-1}. Here, η_{atom} is exactly the atomistic interface width δ_{atom} listed in Table 1, and equals 1.875×10^{-7} cm. The obtained velocity-dependent segregation coefficients are shown in Fig. 6. As can be seen, the solute segregation coefficient $k(V)$ is enhanced when decreasing P from 2000 to 200 cm^3 J^{-1} s^{-1} while keeping the interface width at η_{atom}. However, $k(V)$ is depressed when the interface width increases from η_{atom} to $10\eta_{atom}$ while keeping $P = 200$ cm^3 J^{-1} s^{-1}. According to Fig. 6, the general trend seems to be that a decrease P leads to a higher solute segregation coefficient, while the increase of η results in the lower solute segregation coefficient. It should be borne in mind that Fig. 6 is in fact due to the mixture contribution of P and η because P also varies with η according to Eq. (38). Hence, following Fig. 6, it is possible to reproduce the "experimental data" by adjusting P and η simultaneously.

Two best sets of P and η have been found to fit the "experimental data", namely $1000\eta_{atom} - 0.8$ cm^3 J^{-1} s^{-1} and $10,000\eta_{atom} - 0.1$ cm^3 J^{-1} s^{-1}, as shown in Fig. 7. The solute segregation function $k(V/V_D^B)$ agrees reasonably well with the "experimental data" for $V < 1.5$ m s^{-1} (i.e. $V/V_D^B < 0.6$, where $V_D^B = 2.5$ m s^{-1}). When the interface velocity V is larger than 1.5 m s^{-1}, a large difference between the results from the parabolic model and the "experimental data" appears. It arises due to the nature of the parabolic and hyperbolic models, as pointed out in
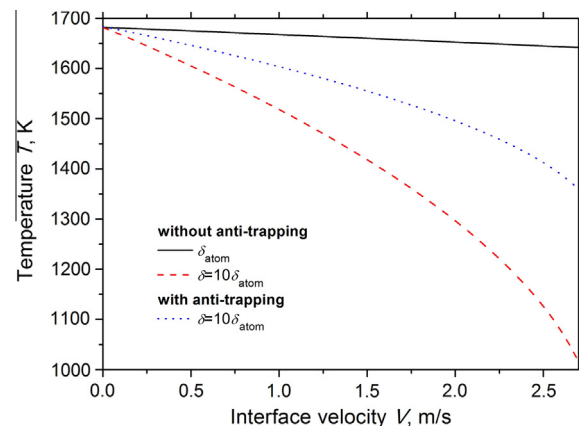

Fig. 4. Kinetics of diffuse interface motion with and without anti-trapping current.
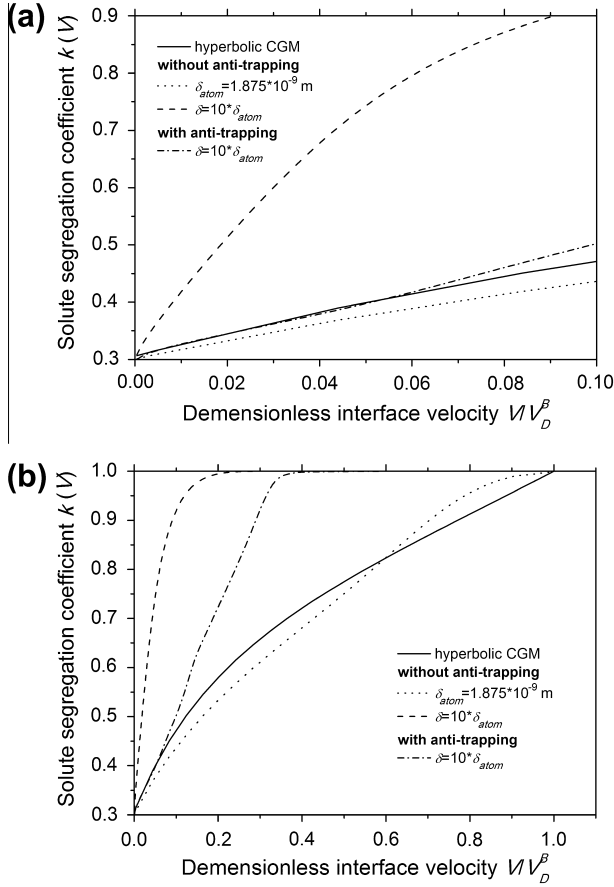
(a)

(b)

Fig. 5. Non-equilibrium solute segregation coefficient $k(V)$ for the Si-0.25 at.% As alloy as predicted by the hyperbolic phase-field model. Results of the modeling are given for the 1.875 nm interface width (dotted line) in comparison with 18.75 nm interface width without anti-trapping (dashed line), and with anti-trapping (dash-dotted line) and hyperbolic CGM [13] (solid line).
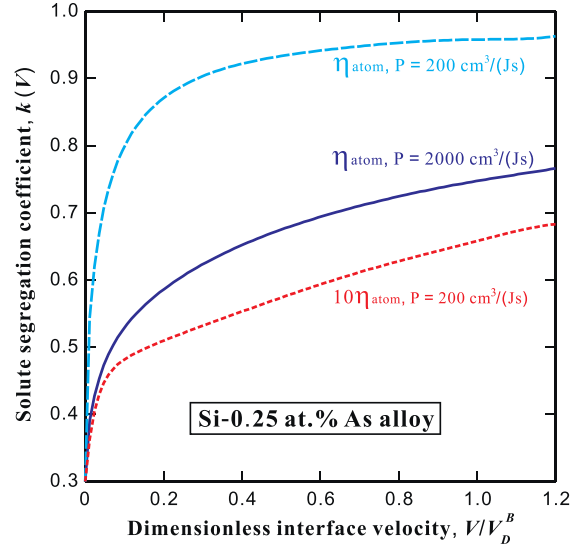

Fig. 6. The effect of interface permeability P and interface width η on the solute segregation coefficient in Si-0.25 at.% As alloy predicted by the parabolic phase-field model with finite interface dissipation. Here, $V_D^B = 2.5$ m s^{-1} and $\eta_{atom} = 1.875 \times 10^{-9}$ m.
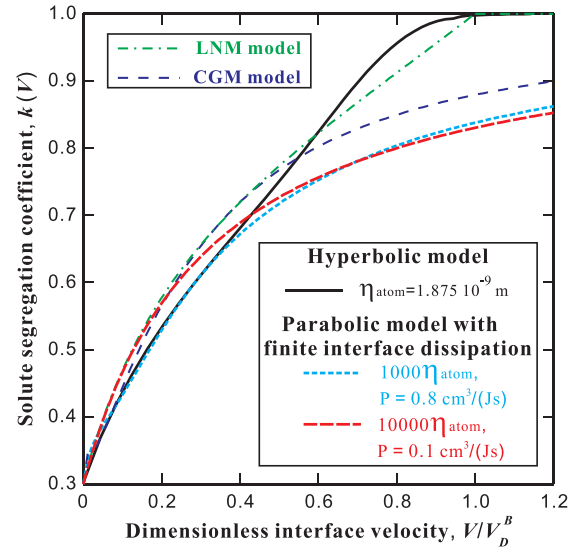

Fig. 7. Comparison among the simulated $k(V)$ with optimal values of P and η due to the parabolic phase-field model, the "experimental data" from the hyperbolic phase-field model (Fig. 5), and the results according to CGM and LNM analytical models.

Section 1. Moreover, the results from the CGM and LNM models are also superimposed in Fig. 7 in order to check the consistency between the results of numerical simulation and those from the analyzed models. As indicated in Fig. 7, the simulated results from the parabolic model agree well with the CGM model over a wide velocity region, but only show good agreement with the LNM model at $V < 1.5$ m s^{-1}. However, a non-trivial point here is that the solute trapping effect during rapid solidification can also be simulated by the parabolic phase-field with interface dissipation on the length scale of μm. This opens the possibility of three-dimensional simulations of rapid solidification which consistently treat solute trapping.

Based on the results of Fig. 7, let us establish a relation for the optimal sets $\eta - P$ with which the "experimental" solute segregation coefficient over the interface velocity range of $V < 1.5$ m s^{-1} can be well reproduced. Moreover, this relation can provide a theoretical basis for choosing reasonable parameters in the further phase-field simulation of rapid solidification. However, with a decrease in the interface width, the simulated solute segregation coefficient

$k(V)$ essentially deviates even at a small interface velocity, $V \approx 0.25$ m s^{-1}. In this case, we can only obtain optimal sets $\eta - P$ that reasonably describe the "experimental" solute segregation coefficients at the interface velocity of $V < 0.25$ m s^{-1}, as demonstrated in Fig. 8. As a result, the optimal sets $\eta - P$ exhibit the following base-10 logarithmic relation (see Fig. 9):

$$\log P = -1.256 \log \eta - 4.560. \qquad (65)$$

Even for this relatively small interface velocity (i.e. $V < 0.25$ m s^{-1}), several regimes of solidification processing
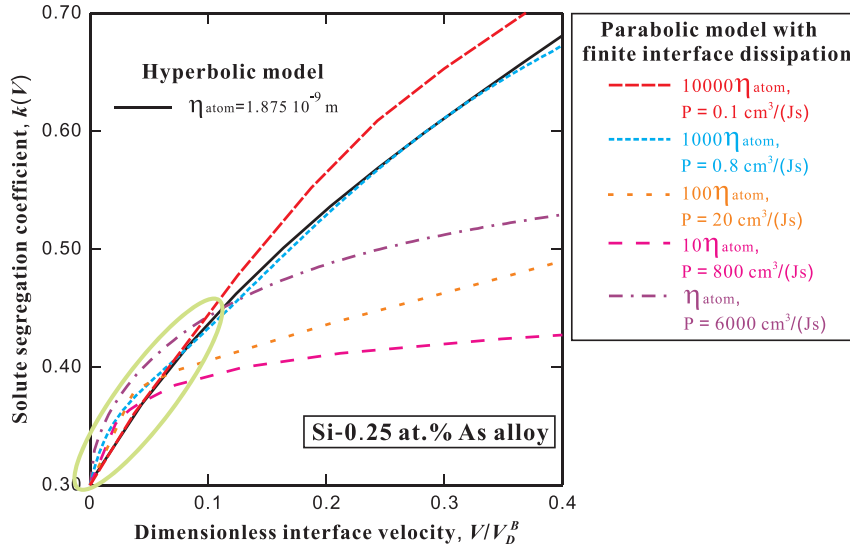
Fig. 8. Comparison between the "experimental" $k(V)$ (Fig. 5) and predictions of the parabolic phase-field model using a series of sets of P and η.
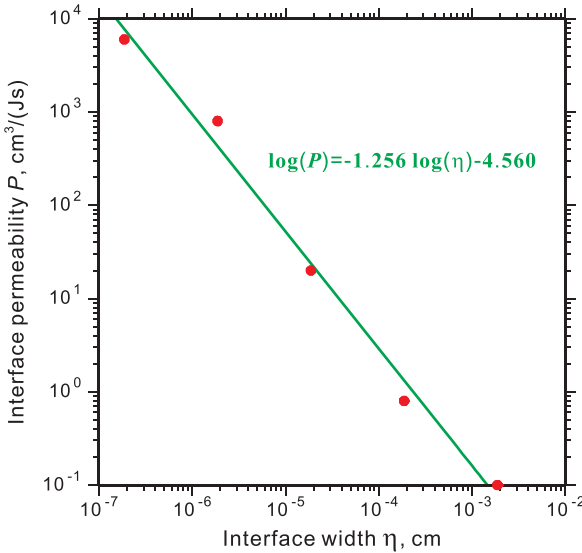

Fig. 9. Relation (65) between the interface permeability P and the interface width η with which the "experimental" $k(V)$ over the velocity range of $V < 0.25$ m s^{-1} can be well reproduced.

can be covered. For instance, the interface velocity for directional solidification in steel ranges from 0.003 to 0.02 m s^{-1}. Therefore, a relation for the sets $\eta - P$ for describing the "experimental data" at the interface velocity range of $V < 0.25$ m s^{-1} still makes sense for the phase-field simulation of various solidification cases with moderate interface velocity. In order to determine the formulation of $f(\eta)$ in Eq. (38), Eq. (65) can be transformed into:

$$P = \frac{2.754 \times 10^{-5}}{\eta^{1.256}} \frac{cm^3}{J\,s}. \tag{66}$$

The M^{int} value can be approximated to be the atomic mobility in bulk liquid phase, M_L, because it is larger than that in the solid phase, M_S, by several orders. Then, M_L can be estimated via the Einstein relation:

$$M_L = \frac{D_L}{RT}, \tag{67}$$

assuming that the present target alloy has dilute solutes. D_L in Eq. (67) can be taken from Table (1), and T can be replaced by the average temperature over the entire simulation range here. With these inputs, the formulation of $f(\eta)$ in Eq. (38) becomes:

$$f(\eta) = \frac{3.91 \times 10^{-4}}{\eta^{1.256}} \frac{1}{cm}. \tag{68}$$

6. Conclusions

The hyperbolic phase-field model and the parabolic model with finite interface dissipation have been utilized to investigate solute trapping during rapid solidification of Si-0.25 at.% As alloy. The solute segregation coefficients simulated by the hyperbolic model with an atomistic interface width were treated as the "experimental data" for Si-0.25 at.% As alloy.

To fit this "experimental data", the interface width η and the interface permeability P were adjusted in the parabolic model with finite interface dissipation in addition to keeping the equivalent material parameters as in the hyperbolic model. The good agreement between the two simulation results at the interface velocities $V < 1.5$ m s^{-1} indicates the possibility of simulations in three spatial dimensions using the parabolic model with finite interface dissipation.

Several sets of optimal interface widths and interface permeabilities that reasonably describe the "experimental data" within the lower interface velocity range were obtained. They were used to evaluate a relation for choosing the appropriate interface width and interface permeability for future numerical simulations.

Appendix A

The concentration equation with an anti-trapping current for the steady-state motion of a diffuse interface can be derived as follows. We start from Eq. (4):

$$\tau_D \frac{\partial^2 c}{\partial t^2} + \frac{\partial c}{\partial t} = \vec{\nabla} \cdot \left[M_c \left(\frac{\partial^2 f}{\partial c^2} \vec{\nabla} c + \frac{\partial^2 f}{\partial c \partial \phi} \vec{\nabla} \phi \right) \right] - \vec{\nabla} \cdot \vec{j}_{AT}, \quad \text{(A.1)}$$

The derivatives with respect to the free energy are

$$\frac{\partial f}{\partial \phi} = -(T - T_A) \frac{\partial s}{\partial \phi} + c \frac{\partial \epsilon}{\partial \phi} + W \frac{\partial g}{\partial \phi}, \quad \text{(A.2)}$$

$$\frac{\partial^2 f}{\partial \phi \partial c} = \frac{\partial \epsilon}{\partial \phi} = -\frac{RT}{v_m} \frac{1 - k_e}{k_e + p(\phi)(1 - k_e)} \frac{\partial p}{\partial \phi}. \quad \text{(A.3)}$$

Introducing the atomic mobility as $M_c = D(\phi) \left(\frac{\partial^2 f}{\partial c^2} \right)^{-1}$ and the diffusion driving force as $\Theta(\phi) = -(1 - k_e)/[k_e + p(\phi)(1 - k_e)]$, we obtain:

$$M_c \frac{\partial^2 f}{\partial c \partial \phi} = c \Theta D(\phi) \frac{\partial p}{\partial \phi}. \quad \text{(A.4)}$$

Using the dimensionless coordinates $x \to (x - Vt)/\delta$ and $t \to tv/\delta^2$, the derivatives in Eq. (A.1) are described by:

$$\frac{\partial c}{\partial x} \to \frac{1}{\delta} \frac{\partial c}{\partial x}, \quad \frac{\partial^2 c}{\partial x^2} \to \frac{1}{\delta^2} \frac{\partial^2 c}{\partial x^2}, \quad \frac{\partial c}{\partial t} \to \frac{v}{\delta^2} \frac{\partial c}{\partial t} - \frac{V}{\delta} \frac{\partial c}{\partial x},$$

$$\frac{\partial^2 c}{\partial t^2} \to \frac{v^2}{\delta^4} \frac{\partial^2 c}{\partial t^2} - 2 \frac{vV}{\delta^3} \frac{\partial^2 c}{\partial t \partial x} + \frac{V^2}{\delta^2} \frac{\partial^2 c}{\partial x^2}.$$

Substituting these derivatives into Eq. (A.1) leads to:

$$\tau_D \frac{v^2}{\delta^4} \frac{\partial^2 c}{\partial t^2} - 2 \frac{vV\tau_D}{\delta^3} \frac{\partial^2 c}{\partial t \partial x} + \frac{V^2 \tau_D}{\delta^2} \frac{\partial^2 c}{\partial x^2} + \frac{v}{\delta^2} \frac{\partial c}{\partial t} - \frac{V}{\delta} \frac{\partial c}{\partial x}$$
$$= \frac{1}{\delta} \frac{\partial}{\partial x} \left[\frac{D(\phi)}{\delta} \frac{\partial c}{\partial x} + c \Theta D(\phi) \frac{\partial p}{\partial \phi} \frac{1}{\delta} \frac{\partial \phi}{\partial x} \right] - \frac{1}{\delta} \frac{\partial j_{AT}}{\partial x}. \quad \text{(A.5)}$$

If the diffuse interface moves with the constant velocity V, then Eq. (A.5) looks like:

$$\frac{\tau_D V^2}{\delta^2} \frac{\partial^2 c}{\partial x^2} - \frac{V}{\delta} \frac{\partial c}{\partial x} = \frac{1}{\delta^2} \frac{\partial}{\partial x} \left[D(\phi) \frac{\partial c}{\partial x} + c \Theta D(\phi) \frac{\partial p}{\partial \phi} \frac{\partial \phi}{\partial x} \right]$$
$$- \frac{1}{\delta} \frac{\partial j_{AT}}{\partial x}. \quad \text{(A.6)}$$

Multiplying Eq. (A.6) by δ^2/D_L and introducing the following characteristic speeds (see Table 1), and

$$V_D^B = \sqrt{\frac{D_L}{\tau_D}}, \qquad V_D^I = \frac{D_L}{\delta},$$

one obtains:

$$\frac{V^2}{(V_D^B)^2} \frac{\partial^2 c}{\partial x^2} - \frac{V}{V_D^I} \frac{\partial c}{\partial x} = \frac{\partial}{\partial x} \left[\frac{D(\phi)}{D_L} \frac{\partial c}{\partial x} + c \Theta(\phi) \frac{D(\phi)}{D_L} \frac{\partial p}{\partial x} \right]$$
$$- \frac{\delta}{D_L} \frac{\partial j_{AT}}{\partial x}. \quad \text{(A.7)}$$

Now, one can consider the anti-trapping flux from Eq. (6) as:

$$j_{AT} = -a \delta (1 - k_e) c_l e^{u(c,\phi)} \frac{\partial \phi}{\partial t}, \quad \text{(A.8)}$$

where

$$u(c, \phi) = \frac{v_m}{RT} (\mu - \mu_{eq})$$
$$= \frac{v_m}{RT} \left[\epsilon(\phi) + \frac{RT}{v_m} \ln c - \epsilon_l - \frac{RT}{v_m} \ln c_l \right]. \quad \text{(A.9)}$$

The function $\epsilon(\phi)$ can be written as:

$$\epsilon(\phi) = \frac{\epsilon_s + \epsilon_l}{2} + p_\epsilon(\phi) \frac{\Delta \epsilon}{2}, \quad \text{(A.10)}$$

where

$$p_\epsilon(\phi) = \frac{2}{\ln k_e} \ln[k_e + p(\phi)(1 - k_e)] - 1, \quad \text{(A.11)}$$

and $\Delta \epsilon$ is given by Eq. (19). After substitution of Eqs. (A.10) and (A.11) into Eq. (A.9) the function $u(c, \phi)$ becomes:

$$u(c, \phi) = \ln \left[\frac{c/c_l}{k_e + p(\phi)(1 - k_e)} \right]. \quad \text{(A.12)}$$

In this case, the anti-trapping current might be written in the form:

$$j_{AT} = -a \delta (1 - k_e) c_l \frac{c/c_l}{k_e + p(\phi)(1 - k_e)} \frac{\partial \phi}{\partial t}$$
$$= a \delta c \Theta(\phi) \frac{\partial \phi}{\partial t}. \quad \text{(A.13)}$$

Using the dimensionless coordinates and substituting the flux (A.13) into Eq. (A.7), we get:

$$- \frac{V}{V_D^I} \frac{dc}{dx} = \frac{d}{dx} \left[\left(\widehat{D}(\phi) - \frac{V^2}{(V_D^B)^2} \right) \frac{dc}{dx} \right]$$
$$+ \frac{d}{dx} \left(\widehat{D}(\phi) c \Theta(\phi) \frac{dp(\phi)}{d\phi} \frac{d\phi}{dx} \right) + a(\phi)$$
$$\times \frac{V}{V_D^I} c \Theta(\phi) \frac{d\phi}{dx}, \quad \text{(A.14)}$$

where we took into account that the functions c and ϕ are the functions of the only variable; therefore, the full derivatives are used. Eq. (A.14) is used for the numerical solution of the solute-trapping problem.

References

[1] Kurz W, Fisher DJ. Fundamentals of solidification. 4th rev. edn. Dürnten: Trans Tech Publications; 1998.

[2] Gollub JP, Langer JS. Rev Mod Phys 1999;71:S396.

[3] Tiaden J, Nestler B, Diepers HJ, Steinbach I. Physica D 1998;115:73.

[4] Kim SG, Kim WT, Suzuki T. Phys Rev E 1999;60:7186.

[5] Kittl JA, Sanders PG, Aziz MJ, Brunco DP, Thompson MO. Acta Mater 2000;48:4797.

[6] Herlach D, Galenko P, Holland-Moritz D. Metastable solids from undercooled melts. Amsterdam: Elsevier; 2007.

[7] Buchmann M, Rettenmayr M. Scripta Mater 2007;57:169.

[8] Aziz MJ. J Appl Phys 1982;53:1158.

[9] Aziz MJ, Kaplan T. Acta Metall 1988;36:2335.

[10] Jackson KA, Beatty KM, Gudgel KA. J Cryst Growth 2004;271:481.

[11] Galenko PK, Sobolev S. Phys Rev E 1997;55:343.

[12] Galenko PK, Danilov DA. Phys Lett A 1997;235:271.

[13] Galenko PK. Phys Rev E 2007;76:031606.

[14] Wheeler AA, Boettinger WJ, McFadden GB. Phys Rev E 1993;47:1893.

[15] Conti M. Phys Rev E 1997;56:3717.

[16] Ahmad NA, Wheeler AA, Boettinger WJ, McFadden GB. Phys Rev E 1998;58:3436.

[17] Danilov D, Nestler B. Acta Mater 2006;54:4659.

[18] Lebedev VG, Abramova EV, Danilov DA, Galenko PK. Int J Mat Res (formerly Z Metallkd) 2010;101:473.

[19] Galenko PK, Abramova EV, Jou D, Danilov DA, Lebedev VG, Herlach DM. Phys Rev E 2011;84:041143.

[20] Penrose O, Fife PC. Physica D 1990;43:44.

[21] Galenko P, Jou D. Phys Rev E 2005;71:046125.

[22] Provatas N, Elder K. Phase-field methods in materials science and engineering. Weinheim: Wiley-VCH; 2010.

[23] Bi Zh, Sekerka R. Physica A 1998;261:95.

[24] Galenko P. Phys Lett A 2001;287:190.

[25] Charach Ch, Fife PC. SIAM J Appl Math 1998;58:1826.

[26] Glasner K. Physica D 2001;151:253.

[27] Echebarria B, Folch R, Karma A, Plapp M. Phys Rev E 2004;70:061604.

[28] Kittl JA, Aziz MJ, Brunco DP, Thompson MO. J Cryst Growth 1995;148.

[29] Yang Y, Humadi H, Buta D, Laird BB, Sun D, Hoyt JJ, et al. Phys Rev Lett 2011;107:025505.

[30] Steinbach I, Zhang L, Plapp M. Acta Mater 2012;60:2689.

[31] Eiken J, Böttger B, Steinbach I. Phys Rev E 2006;73:066122.

[32] Steinbach I. Model Simul Mater Sci Eng 2009;17:073001.

[33] Karma A. Phys Rev Lett 2001;87:115701.

[34] Lebedev VG, Sysoeva AV, Galenko PK. Phys Rev E 2011;83:026705.

[35] Vinet B, Magnusson L, Fredriksson H, Desre PJ. J Colloid Interface Sci 2002;255:363.

[36] Zhang L, Steinbach I. Acta Mater 2012;60:2702.

[37] Galenko PK, Abramova EV, Herlach DM. Discret Contin Dyn S 2011;(Supplement 1):457.